

<https://doi.org/10.1038/s43246-021-00185-4>

OPEN

## Evolution of defect formation during atomically precise desulfurization of monolayer MoS<sub>2</sub>

Jong-Young Lee<sup>1,2,12</sup>, Jong Hun Kim<sup>1,2,3,12</sup>, Yeonjoon Jung<sup>1</sup>, June Chul Shin<sup>1</sup>, Yangjin Lee<sup>4,5</sup>, Kwanpyo Kim<sup>4,5</sup>, Namwon Kim<sup>1,6</sup>, Arend M. van der Zande<sup>7</sup>, Jangyup Son<sup>8,9</sup>✉ & Gwan-Hyoung Lee<sup>1,2,10,11</sup>✉

Structural symmetry-breaking is a key strategy to modify the physical and chemical properties of two-dimensional transition metal dichalcogenides. However, little is known about defect formation during this process. Here, with atomic-scale microscopy, we investigate the evolution of defect formation in monolayer MoS<sub>2</sub> exposed indirectly to hydrogen plasma. At the beginning of the treatment only top-layer sulfur atoms are removed, while vacancies and the molybdenum atomic layer are maintained. As processing continues, hexagonal-shaped nanocracks are generated along the zigzag edge during relaxation of defect-induced strain. As defect density increases, both photoluminescence and conductivity of MoS<sub>2</sub> gradually decreases. Furthermore, MoS<sub>2</sub> showed increased friction by 50% due to defect-induced contact stiffness. Our study reveals the details of defect formation during the desulfurization of MoS<sub>2</sub> and helps to design the symmetry-breaking transition metal dichalcogenides, which is of relevance for applications including photocatalyst for water splitting, and Janus heterostructures.

<sup>1</sup> Department of Material Science and Engineering, Seoul National University, Seoul 08826, Korea. <sup>2</sup> Research Institute of Advanced Materials, Seoul National University, Seoul 08826, Korea. <sup>3</sup> Department of Materials Science and Engineering, Yonsei University, Seoul 03722, Korea. <sup>4</sup> Department of Physics, Yonsei University, Seoul 03722, Korea. <sup>5</sup> Center for Nanomedicine, Institute for Basic Science (IBS), Seoul 03722, Korea. <sup>6</sup> Ingram School of Engineering, Texas State University, San Marcos 78666 TX, USA. <sup>7</sup> Department of Mechanical Science and Engineering, University of Illinois Urbana-Champaign, Urbana 61801 IL, USA. <sup>8</sup> Functional Composite Materials Research Center, Korea Institute of Science and Technology (KIST), Jeonbuk 55324, Korea. <sup>9</sup> Division of Nano and Information Technology, KIST School University of Science and Technology (UST), Jeonbuk 55324, Korea. <sup>10</sup> Institute of Engineering Research, Seoul National University, Seoul 08826, Korea. <sup>11</sup> Institute of Applied Physics, Seoul National University, Seoul 08826, Korea. <sup>12</sup>These authors contributed equally: Jong-Young Lee, Jong Hun Kim. ✉email: [jayson@kist.re.kr](mailto:jayson@kist.re.kr); [gwanlee@snu.ac.kr](mailto:gwanlee@snu.ac.kr)

**S**urface/defect engineering of two-dimensional (2D) materials by laser exposure, ion irradiation, and plasma treatment has been studied actively because the modification of the surface can totally change the properties of 2D materials due to large surface-to-volume ratio<sup>1–13</sup>. Such a surface/defect-engineered 2D materials have a potential for high-performance field-effect transistor<sup>13–15</sup>, sensor<sup>16</sup>, and catalyst<sup>17–19</sup>. Among various methods for defect generation, the plasma treatment has shown great potential for transition metal dichalcogenides (TMDs), such as MoS<sub>2</sub>, MoTe<sub>2</sub>, and WSe<sub>2</sub>, due to high controllability and uniformity, leading to chemical functionalization, heteroatom doping, defect generation, and etching<sup>12,20–23</sup>. Recently, it was reported that Janus-type membrane<sup>24,25</sup> of MoSSe and WSSe can be fabricated by selenizing the hydrogenated top surface<sup>26,27</sup>. Moreover, several studies have shown that defects in MoS<sub>2</sub> can enhance catalytic performance for water splitting and hydrogen evolution reaction<sup>17,22,23,28–31</sup>. Nevertheless, the structural evolution of MoS<sub>2</sub> during hydrogen plasma treatment was not studied due to the high reactivity of hydrogen plasma with MoS<sub>2</sub> and the instability of plasma-treated MoS<sub>2</sub>. Thus, systematic study on the structure and properties of plasma-treated MoS<sub>2</sub> is required to develop a method to slightly modify the surface or controllably generate a specific density of defects in three-atom-thick MoS<sub>2</sub><sup>32</sup>.

Here, we investigated the evolution of defect formation in monolayer MoS<sub>2</sub> during exposure to low-energy indirect hydrogen plasma, which enables atomic precision etching. The sulfur atoms of top layer in three-atom-thick MoS<sub>2</sub> were able to be removed with preserved molybdenum atomic layer and no damage to sulfur atoms of bottom layer. The sulfur vacancies started to form in the beginning of plasma treatment and became dominant up to  $1.58 \times 10^{14} \text{ cm}^{-2}$  (for 40 min-treated sample) as the plasma treatment proceeded, resulting in plasma-treated MoS<sub>2</sub> with preserved 2H-structure. Finally, nanocracks were generated along the zigzag orientation of MoS<sub>2</sub> to relax the defect-induced biaxial tensile strain. These nanocracks appeared when more than 50% of sulfur atoms were removed from the top layer. The optical, electrical, and mechanical properties of the plasma-treated MoS<sub>2</sub> were also explored to correlate them to the structural changes of MoS<sub>2</sub>. The photoluminescence (PL) intensity gradually decreased during plasma treatment and it was finally quenched. The conductivity of MoS<sub>2</sub> also decreased by two orders of magnitude due to high density of defects, in contrast to theoretically expected metallic property of MoSH. Furthermore, the lateral tip-surface contact stiffness measured by lateral force microscopy increased by ~50% after plasma treatment. Our work shows that atomic precision etching is possible and the properties of MoS<sub>2</sub> can be controlled by surface/defect engineering.

## Results and discussion

**Evolution of defects in plasma-treated MoS<sub>2</sub>.** We used a home-built remote hydrogen plasma system, consisting of three ring-shaped electrodes and a low-frequency plasma generator, to desulfurize only the topmost atomic layer of monolayer MoS<sub>2</sub> in an atomically precise and physically mild manner (Fig. 1a, b)<sup>32–34</sup>. The plasma was generated at the center of three electrodes and monolayer MoS<sub>2</sub> crystals grown by chemical vapor deposition (CVD)<sup>35</sup> were placed away from the plasma ignition area to avoid direct ion bombardment (see the “Methods” Section for details of the MoS<sub>2</sub> growth and remote hydrogen plasma treatment). To investigate the structural change in the desulfurized MoS<sub>2</sub> with hydrogen plasma treatment, we measured Raman spectra of MoS<sub>2</sub>, which is sensitive to perturbation of crystal structure induced by deformation and doping (Fig. 1c). The Raman spectra of hydrogen plasma-treated MoS<sub>2</sub> (HP-MoS<sub>2</sub>) showed significant shifts and broadening of E' and A<sub>1'</sub> vibration

modes, which are attributed to strain and doping<sup>10</sup>. In addition, disorder-related Raman peaks emerged as indicated by transversal optical, longitudinal optical, and out-of-plane optical modes at 342, 366, and 413 cm<sup>-1</sup>, respectively, in Fig. 1c<sup>36</sup>. As summarized in Fig. 1d, the E' peak, in-plane vibration mode of Mo-S bond, red-shifted from 382.2 to 371.6 cm<sup>-1</sup>, meanwhile the A<sub>1'</sub> peak, out-of-plane vibration mode, blue-shifted from 402.6 to 409.5 cm<sup>-1</sup>. As a result, the frequency difference between two peaks increased from 20.4 to 37.9 cm<sup>-1</sup>. Such notable peak shifts correspond to the formation of sulfur vacancies<sup>37</sup>. High density of sulfur vacancies at the top layer of MoS<sub>2</sub> weakens the in-plane vibration in the Mo-S bonds, leading to a weaker restoring force constant and lower phonon frequency of E'. For frequency of A<sub>1'</sub>, restoring force constant also decreased with sulfur vacancies. However, the removal of top sulfur atoms allows out-of-plane vibration of static molybdenum atoms, then the resonance frequency of A<sub>1'</sub> raises as we observed. Also, the intensities of two peaks gradually decreased after plasma treatment, which attribute to the degradation of MoS<sub>2</sub><sup>22,38–41</sup>.

**Atomic structure and defects in MoS<sub>2</sub> after treatment.** To further examine the atomic structure of HP-MoS<sub>2</sub>, we utilized transmission electron microscopy (TEM) and high-angle annular dark-field scanning transmission electron microscopy (HAADF-STEM). The CVD-grown MoS<sub>2</sub> samples were transferred onto the graphene-coated holey carbon TEM grid, followed by the hydrogen plasma treatment. The graphene supporting film enables high-resolution imaging of the transferred MoS<sub>2</sub> by TEM due to the dissipation of electrostatic charging and heating under e-beam (see details in the “Methods” Section)<sup>42</sup>. In the HAADF-STEM, the image contrast is determined by the Z-contrast mechanism,  $I \propto Z^n$ , where  $I$  and  $Z$  are image contrast and atomic number. The index ( $n$ ) is the number between 1 and 2, which depends on the scattering angles<sup>43</sup>. In the MoS<sub>2</sub> supported on graphene-coated TEM grid, the molybdenum atoms with  $Z = 42$  look brighter than the sulfur atoms with  $Z = 16$  and carbon atoms with  $Z = 12$ , so that the graphene membrane can be ignored in our images. The HAADF-STEM images of the Fig. 2a, b show that the as-grown MoS<sub>2</sub> has the hexagonal structure of 2H-phase with small number of sulfur vacancies as indicated by yellow circles. The estimated density of sulfur vacancies in the as-grown MoS<sub>2</sub> was  $1.60 \times 10^{13} \text{ cm}^{-2}$ , which shows the high quality of the sample, compared to MoS<sub>2</sub> samples used in other works<sup>44–46</sup>. The density of vacancies was estimated by the direct counting in obtained images to determine a quantitative value. Meanwhile, the HP-MoS<sub>2</sub> treated for 40 min showed significantly increased density of sulfur vacancies ( $1.58 \times 10^{14} \text{ cm}^{-2}$ ) as shown in Fig. 2c, d. The HP-MoS<sub>2</sub> showed mainly two types of vacancies at sulfur positions, monosulfur (V<sub>S</sub>) and disulfur vacancies (V<sub>S2</sub>, indicated by green circles). Note that the calculated formation energy of V<sub>S2</sub> is relatively high as 4.14 eV<sup>45</sup>. Therefore, V<sub>S2</sub> is formed by the generation of V<sub>S</sub> in topmost layer while V<sub>S</sub> already resided in the bottom layer, not directly generated by hydrogen plasma treatment (See Supplementary Fig. 1 for schematic diagram of V<sub>S2</sub> formation). In addition, the sulfur vacancies are aligned preferentially along the zigzag orientation (indicated by red arrows in Fig. 2c) as expected by theoretical calculation<sup>47–49</sup>. The higher magnification color-contrasted HAADF-STEM images of the as-grown MoS<sub>2</sub> (Fig. 2b) and HP-MoS<sub>2</sub> (Fig. 2d) clearly show that the number of sulfur vacancies increased after hydrogen plasma treatment. From the line intensity profiles of the HAADF-STEM images (Fig. 2e), the local sites and types of sulfur vacancies were identified by using the different local intensities of V<sub>S</sub> and V<sub>S2</sub>. For statistical analysis, we extract the local intensities at the atomic sites of Mo and S as shown in the histograms of Fig. 2f.

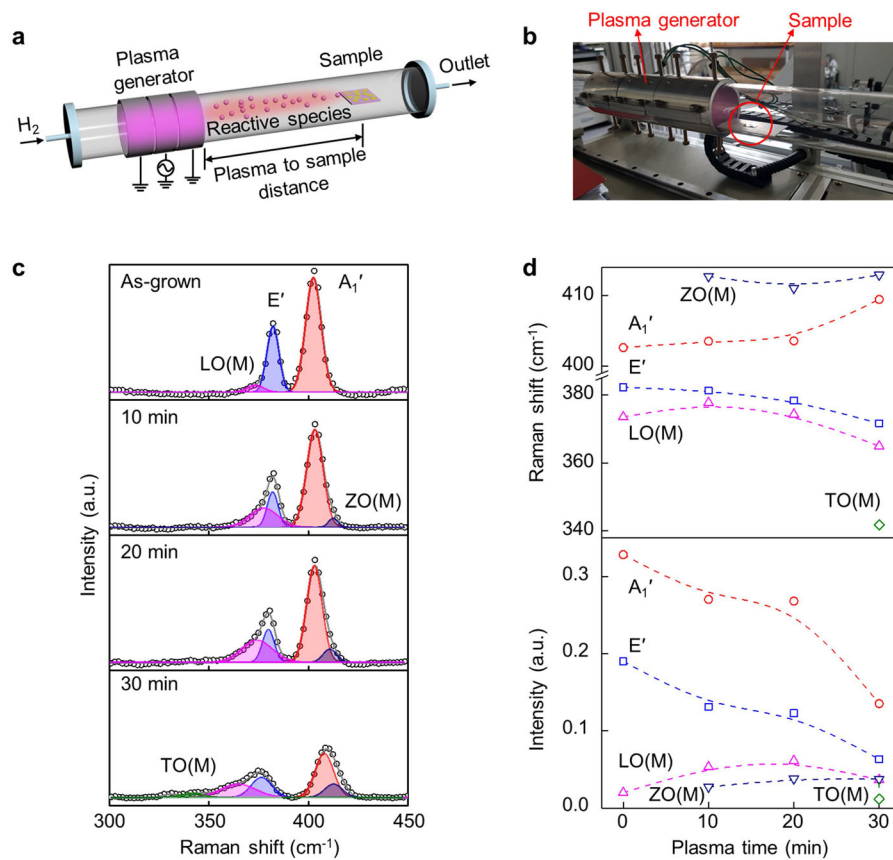


**Fig. 1 Exposure of hydrogen plasma to MoS<sub>2</sub> using remote hydrogen plasma treatment system.** Schematics (a) and photograph (b) of the home-built remote hydrogen plasma system. c Raman spectra fitting result of MoS<sub>2</sub> and HP-MoS<sub>2</sub>. d The frequencies (top panel) and intensities (bottom panel) of E', A<sub>1</sub>', LO, ZO, and TO modes.

The Mo and S atoms showed two distributions around 1.5 and 1.0, respectively. The local intensity distributions of the Mo atoms in the as-grown MoS<sub>2</sub> and HP-MoS<sub>2</sub> showed negligibly small difference, meanwhile the local intensity of two S atoms (S<sub>2</sub>) showed a significant decrease due to formation of the sulfur vacancies. The increased distribution peak of V<sub>S</sub> is located at 0.6 in the histograms. Even though a few V<sub>S2</sub> were observed (very small intensity at 0.2), it is not clear that those are generated during hydrogen plasma treatment since the as-grown MoS<sub>2</sub> probably has some missing sulfur atoms at bottom layer before the hydrogen plasma treatment. Nevertheless, it should be noted that V<sub>S</sub> significantly increased after hydrogen plasma treatment. However, it is still difficult to verify the presence of hydrogen atoms bonded to Mo atoms (Mo-H) or sulfur atoms (S-H), which were reported as a result of hydrogenation<sup>26,50</sup>.

**Chemical characterization of the plasma-treated MoS<sub>2</sub>.** We performed chemical composition analysis using Auger electron spectroscopy (AES) and time-of-flight secondary ion mass spectroscopy (ToF-SIMS) to confirm the relationship between crack formation and the chemical composition. As shown in Fig. 3a, the AES features around 156 (S LVV) and 190 eV (Mo MVV) for the MoS<sub>2</sub> samples. The intensity of the peak at S decreases while that of Mo peak is constant, implying that sulfur vacancies were produced without molybdenum vacancies, as observed in TEM and STEM. In the AES result, chemical compositions were extracted based on peak-to-valley height proportional to the atomic concentration and sensitivity factor<sup>51</sup>. Figure 3b shows that the calculated atomic ratio (S/Mo) of the as-grown MoS<sub>2</sub> is ~2, close to the ideal stoichiometry of MoS<sub>2</sub>. However, after

treatment, the S/Mo ratio gradually decreased to 1.60 and 1.15 for HP-MoS<sub>2</sub> (10 min) and HP-MoS<sub>2</sub> (30 min), respectively. The ToF-SIMS depth profiling of the as-grown MoS<sub>2</sub> and HP-MoS<sub>2</sub> (30 min) was performed with Cesium (Cs) sputtering (0.5 keV) to reveal the vertical position of sulfur vacancies. Figure 3c shows the ToF-SIMS negative spectra of sulfur (S<sup>-</sup>) as a function of the elapsed sputtering time. The intensity of sulfur in the as-grown MoS<sub>2</sub> is higher than HP-MoS<sub>2</sub> (30 min) at early sputtering time and difference between them becomes negligible, indicating that the indirect hydrogen plasma removes only top sulfur layer of the three-atom-thick MoS<sub>2</sub> as depicted in the inset of Fig. 3c.

**Formation of nanocracks in the plasma-treated MoS<sub>2</sub>.** In the HP-MoS<sub>2</sub> (30 min), we observed the formation of nanocracks as shown in Fig. 4. Although the surface of HP-MoS<sub>2</sub> (30 min) looked smooth and clean in the optical microscopic image of Fig. 4a, many line patterns with a hexagonal shape were observed in the dark-field optical microscopic image as shown in Fig. 4b. These line patterns were investigated by using atomic force microscopy (AFM), scanning electron microscope (SEM), and TEM as shown in Fig. 4c–h. The line patterns were not detected in the AFM topography image of Fig. 4c, probably due to the smaller width of the line rather than AFM tip radius and roughness of the SiO<sub>2</sub> substrate. However, the AFM friction image of Fig. 4d showed clear line patterns due to the lower friction of line regions. The SEM image of Fig. 4e clearly shows that the hexagonal patterns are 1 μm in size and angle distribution of the lines relative to the edge of the MoS<sub>2</sub> crystal has preferential orientations of 0°, 60°, and 120° as summarized in Fig. 4f, which indicates that the line patterns are associated with

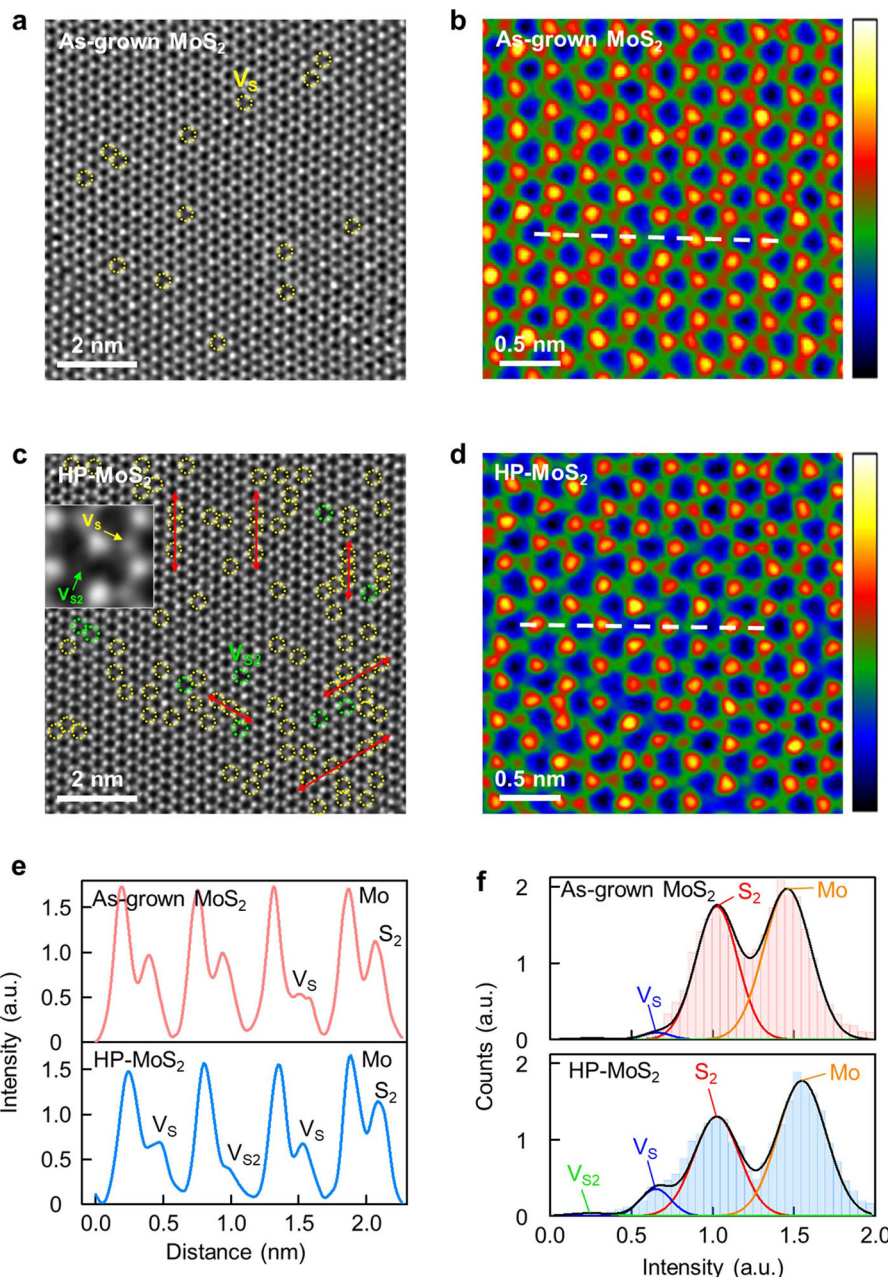


**Fig. 2 Observation of atomic structure of MoS<sub>2</sub> and HP-MoS<sub>2</sub> using STEM.** STEM images of **a**, **b** as-grown MoS<sub>2</sub> and **c**, **d** HP-MoS<sub>2</sub>. Yellow and green circles indicate the position of monosulfur (V<sub>s</sub>) and disulfur vacancies (V<sub>s2</sub>), respectively. Red arrows indicate sulfur vacancies along zigzag orientation of MoS<sub>2</sub>. The inset shows enlarged STEM images and structure of V<sub>s</sub> and V<sub>s2</sub>. **e** Intensity profiles obtained along the white dashed lines in **b** and **d**. **f** Distribution of intensities at S and Mo sites extracted from STEM images. The curve lines are Gaussian fitting curves to data.

the crystallographic orientation of the MoS<sub>2</sub>. For TEM imaging of HP-MoS<sub>2</sub>, we treated hydrogen plasma followed by transferring MoS<sub>2</sub> sample onto a silicon nitride TEM grid. The TEM image of Fig. 4g shows that a narrow lines (indicated by yellow arrows) are between two regions (termed 'A' and 'B'). The selected area electron diffraction pattern in the inset of Fig. 4g shows that two regions of A and B have the same hexagonal symmetry, indicating that two regions are separated from the MoS<sub>2</sub> grains, not misaligned grains. On the other hand, two-line patterns are aligned along the zigzag direction of the MoS<sub>2</sub> as indicated by red arrows. The HAADF-STEM image of Fig. 4h clearly shows that the line between A and B regions is a nanocrack with a width of ~10 nm. However, the edges of the crack are rough, compared to highly sharp edges of chemically etched MoS<sub>2</sub><sup>22</sup>.

**Relaxation of defect-induced strain and formation of nanocracks.** To investigate the strain effect on the HP-MoS<sub>2</sub> (30 min), we analyzed the Raman spectra of cracked and uncracked regions as shown in Fig. 5a. The peak positions of E' and A<sub>1</sub>' modes are influenced by doping and strain<sup>52–54</sup>. Both regions showed the increased separation between the E' and A<sub>1</sub>' ( $\Delta \sim 33 \text{ cm}^{-1}$ ) after plasma treatment due to the formation of vacancies as we discussed. The cracked region showed blue shifts of two Raman peaks compared to those of the uncracked region as shown in Fig. 5b. This peak shift in defective MoS<sub>2</sub> has been explained by strain effect<sup>53,54</sup>. The blue shift of the Raman peaks can be attributed to a decrease of bond length under compressive strain and increase of the force constant. On the other hand, red shift can be result from increasing tensile strain, attributing to the

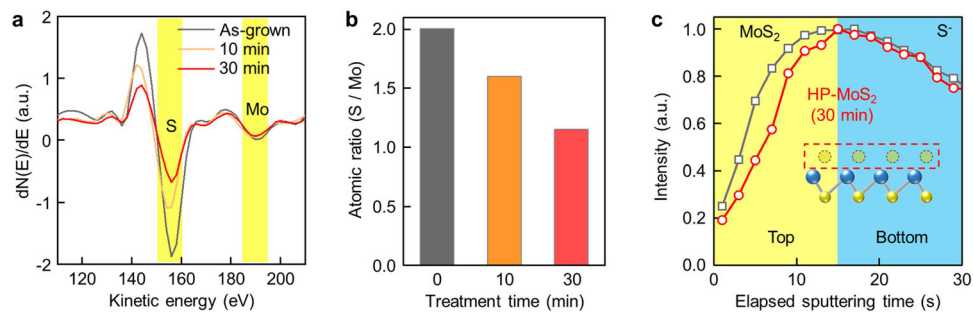


**Fig. 3 Chemical composition of MoS<sub>2</sub> after desulfurization.** **a** Differential energy distribution spectra of Auger electrons detected from MoS<sub>2</sub> and HP-MoS<sub>2</sub>. **b** The atomic ratio of sulfur-to-molybdenum within samples. **c** ToF-SIMS depth profile of sulfur ion achieved from MoS<sub>2</sub> and HP-MoS<sub>2</sub>. Inset shows the atomic structure of MoS<sub>2</sub> after removing top-sulfur layer.

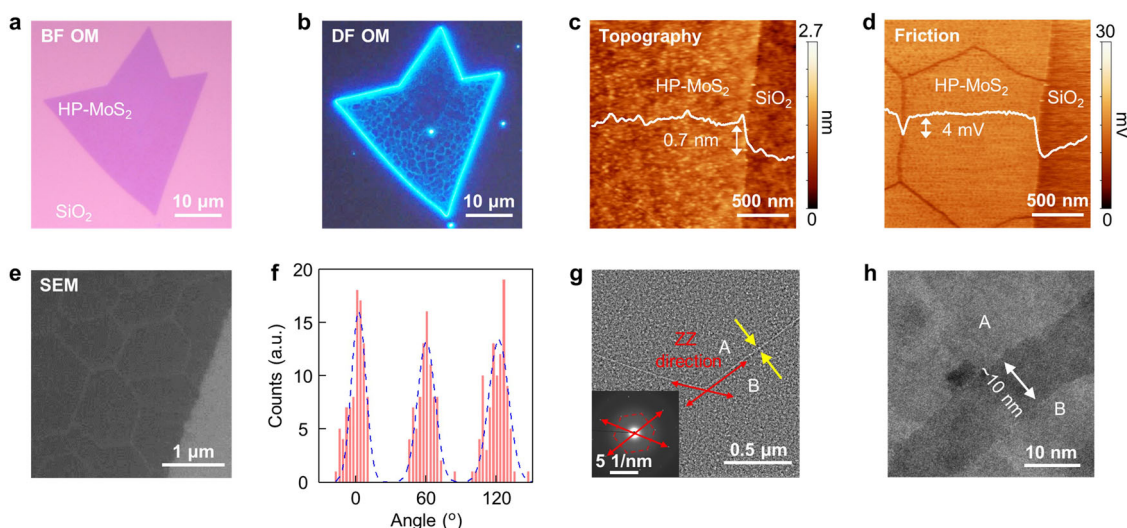


**Fig. 4 Microscopic observation of nanocracks in HP-MoS<sub>2</sub> (30 min).** Bright (a) and dark (b) field optical microscopic image, SEM image (c), topography (d), and friction map (e) obtained from HP-MoS<sub>2</sub> (30 min), respectively. **f** Histogram of angle difference between lines and edge of the crystal. **g** TEM images obtained from the cracked region. Yellow arrows indicate the location of the crack between 'A' and 'B', and red arrows indicate the zigzag (ZZ) lattice directions of HP-MoS<sub>2</sub>. Inset shows SAED patterns achieved from a region containing both 'A' and 'B'. **h** STEM image obtained nearby linear region, showing ~10 nm of gap between two regions.

reduction of the force constant in MoS<sub>2</sub>. Thus, cracked region undergoes less tensile strain than uncracked region, meaning that nanocracks generate during the relaxation of tensile strain. The alignment of vacancies (Fig. 2c) is an intermediate step between vacancies and cracks, and transition occurs when the strain or defect size exceeds the certain value. We assumed that the crack generates after more than 50% of sulfur atoms in the topmost layer is etched (S/Mo value between 1.5 and 1.0, which is calculated from AES result), as a result of relaxation of strong defect-induced strain. According to our observations, the etching process for the top-sulfur atoms and the following crack formation are speculated as depicted in Fig. 5c. First, atomic defects are generated randomly in topmost surface of monolayer MoS<sub>2</sub> after hydrogen plasma treatment. As we discussed above, the defect is thought to dominantly consist of sulfur vacancies (V<sub>S</sub>, V<sub>S2</sub>). After longer treatment, sulfur vacancies preferentially generate along zigzag orientation as shown in the third image. Sequentially, when the half of top sulfur atoms is etched, cracks generate along zigzag orientation during relaxation of defect-induced strain. Furthermore, the HP-MoS<sub>2</sub> (180 min) was separated into small islands with scrolled edges (for optical and AFM image see Supplementary Fig. 2). The low S/Mo ratio of 0.64 indicates that even bottom sulfur atoms of MoS<sub>2</sub> are etched (Supplementary Fig. 3 contains AES spectra).

**Evolution of optical and electrical properties.** To investigate the effect of defects on the optical properties, the PL spectra of the MoS<sub>2</sub> were measured after plasma treatment (Fig. 6a). Two emission peaks at ~1.84 and ~2.0 eV, corresponding to A and B excitonic transitions, were rapidly decreased and finally quenched as shown in the inset of Fig. 6a as the plasma treatment proceeded. To understand the origin of PL spectral change, we used Gaussian fits to extract the contribution of excitons as shown in Fig. 6b. The PL spectra were deconvoluted into four peaks of A-exciton (A), negatively charged trion (A<sup>-</sup>), B-exciton (B), and defect-induced exciton (X<sub>D</sub>)<sup>55</sup>. The A-peak and A<sup>-</sup>-peak were dominant in the PL spectra, and B-peak was also evident in emission, while X<sub>D</sub> was absent for as-grown MoS<sub>2</sub>. By contrast, B-peak became dominant and X<sub>D</sub> appeared after treatment. This behavior results from the increase of non-radiative recombination due to a high density of defects<sup>56,57</sup>. In as-grown MoS<sub>2</sub>, radiative recombination dominantly occurs at ground state, a strong A-peak and weak B-peak are expected. In HP-MoS<sub>2</sub>, non-radiative recombination becomes common due to defects and reduces effective A-exciton lifetime, while B-exciton lifetime is moderately impacted<sup>57</sup>. Also, A<sup>-</sup>-peak decreases together as A-peak decreases. The energy of excitons shifts to lower energy level with increasing treatment time. The PL shift during treatment can be explained based on strain effect as we observed in Raman spectroscopy<sup>58</sup>.

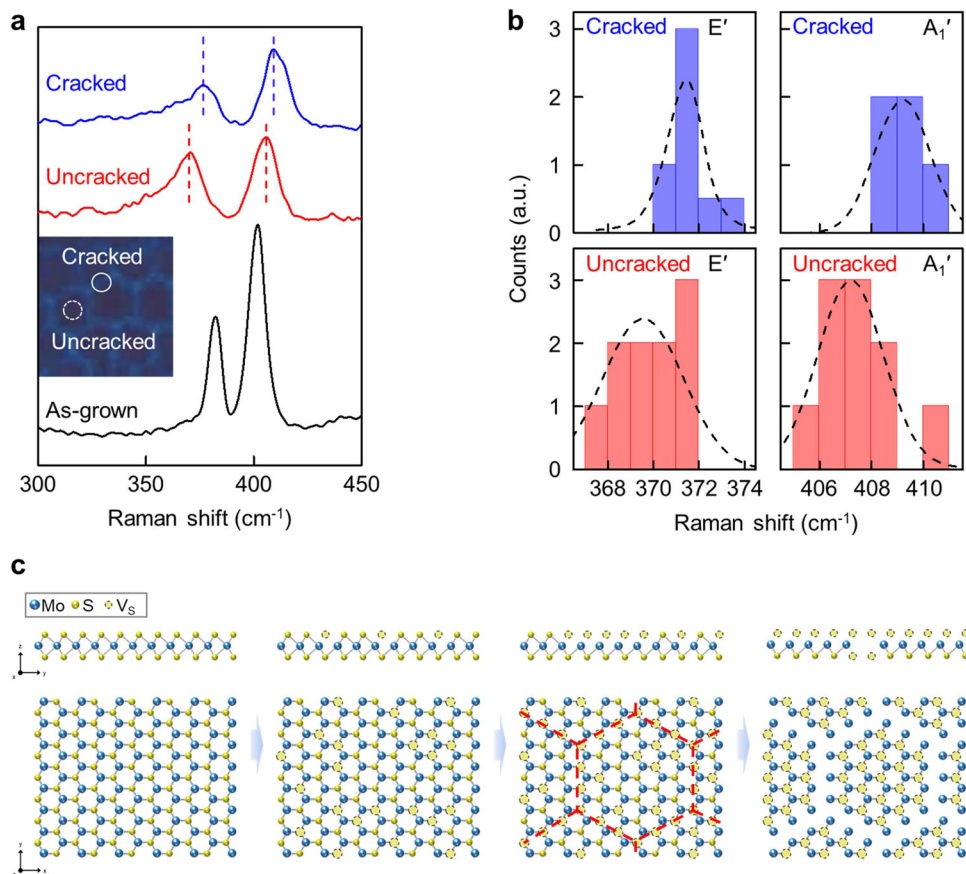


**Fig. 5 Strain-related evolution of Raman spectra and formation of cracks.** Representative Raman spectra (a) and E', A<sub>1'</sub> peak positions (b) extracted from cracked and uncracked region in HP-MoS<sub>2</sub> (30 min). The inset in a shows two spots for Raman measurement. c The schematic diagram of the one-atom-thick surface engineering process. The red lines highlight the location of sulfur vacancies along zigzag orientation.

The energy states of the valence band and conduction band originate from the 3p orbital of S atoms and 4d orbital of Mo atoms. The strain effect leads interatomic distance change between the Mo and S atoms, and further modifies the overlap between those orbitals, which results in energy shift in band gap. Tensile strain causes the reduction of the distance between the S atoms and the increase of the distance between Mo and S atoms, which induces a rise of the energy at the top of the valence band near the  $\Gamma$  point and at the bottom of the conduction band between the  $K$  and the  $\Gamma$  points and results reducing band gap<sup>59</sup>. The evolution of spectral weight and photon energy of each emission following treatment time is summarized in Fig. 6c. The change of electrical properties was investigated by plasma-treating the MoS<sub>2</sub> FET as shown in the inset of Fig. 6d. We fabricated PMMA window only over the channel area to prevent damage to the metal contact area. The output curves ( $I_{ds}$ - $V_{ds}$ ) show that the treated MoS<sub>2</sub> becomes more resistive with increasing treatment time (Fig. 6d). Note that the hydrogen-based bandgap modulation of MoS<sub>2</sub>, such as hydrogenation and vacancy generation, has been studied by experimental and computational method<sup>50,60</sup>. The hydrogenation of MoS<sub>2</sub> includes the formation of S-H bond by surface adsorption and atomic substitution of sulfur to hydrogen, showing bandgap reduction or semiconductor to metal transition. Similarly, it has been reported that sulfur vacancies act as an electron donors and induce n-doping of MoS<sub>2</sub><sup>61,62</sup>. However, unlike the previous results, we observed the decreasing conductivity of MoS<sub>2</sub>-FET, which is presumed to be due to the convolution of defect and strain. The sulfur vacancies and strain-induced cracks in HP-MoS<sub>2</sub> act as electron-hole scattering sites, which decrease

the conductivity of carriers, and finally show insulating behavior after degradation of MoS<sub>2</sub>.

**Mechanical properties of the plasma-treated MoS<sub>2</sub>.** To verify the tribological change in the HP-MoS<sub>2</sub>, the local frictional properties of the HP-MoS<sub>2</sub> were characterized using AFM. Fig. 7a-c presents the high-resolution topography and lateral force images of the as-grown MoS<sub>2</sub> and HP-MoS<sub>2</sub> samples treated for 10 and 30 min, respectively. The atomic-scale sawtooth pattern of the as-grown MoS<sub>2</sub> was clearly observed in both topography and lateral force images, indicative of high crystallinity and uniformity of the as-grown MoS<sub>2</sub>. As shown in the fast Fourier transform (FFT) of the lateral force image of Fig. 7d, the as-grown MoS<sub>2</sub> exhibits a set of hexagonal spots with a distance of  $\sim 0.3$  nm, close to the lattice parameter of MoS<sub>2</sub><sup>63</sup>. This indicates that the single stick-slip occurs by periodic potential wells consisting of adjacent top-sulfur atoms<sup>64,65</sup>. The onset of stick-slip occurs when the value,  $\eta = \frac{2\pi E_0}{ka^2}$  becomes larger than 1<sup>66</sup>. Here,  $E_0$ ,  $k$ , and  $a$  denote the barrier of potential well, effective contact stiffness, and lattice space, respectively. The  $E_0$  reflects interaction between tip and sample made from every lattice point. Therefore, the emergence of regular sawtooth signal in Fig. 7a implies that the as-grown MoS<sub>2</sub> contains constant energy barrier and lattice spacing together with low contact stiffness, meeting the condition of  $\eta > 1$ . On the other hand, HP-MoS<sub>2</sub> contains irregular energy barrier and large lattice spacing in defective sites, meeting the condition of  $\eta < 1$  and losing periodic sawtooth signal. Meanwhile, the FFT images of the HP-MoS<sub>2</sub> show just two

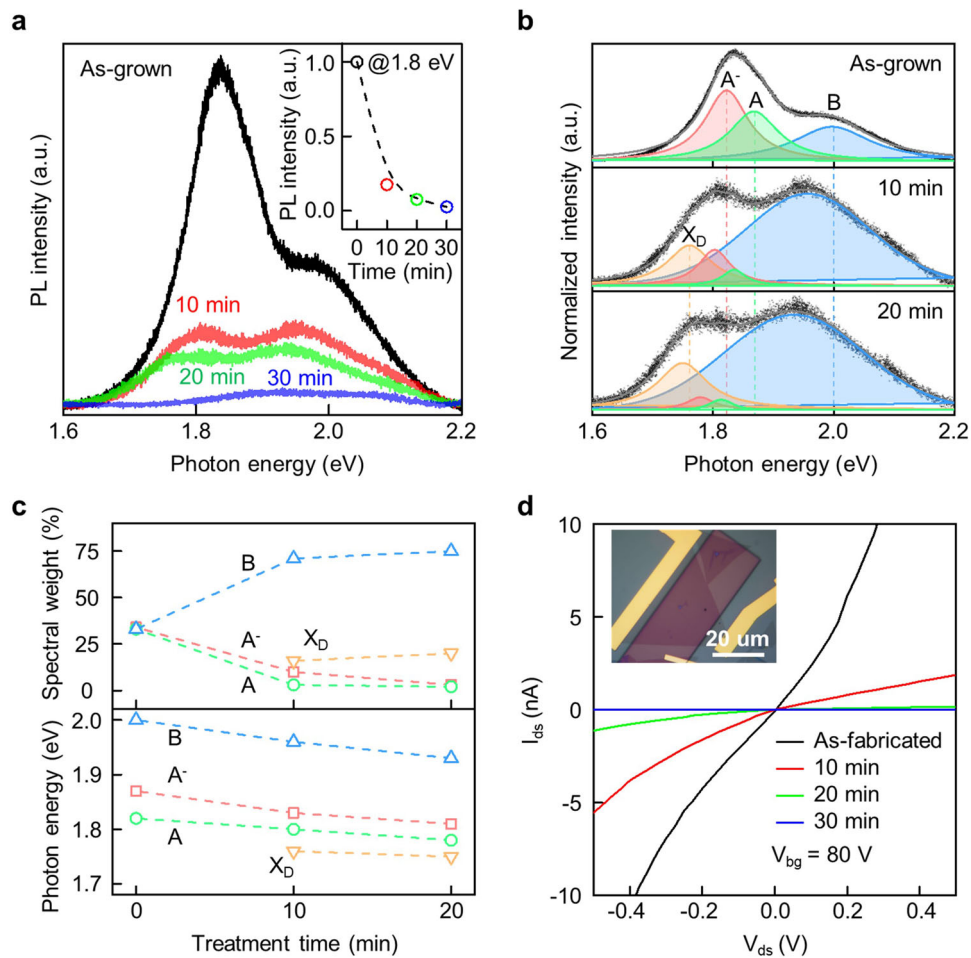


**Fig. 6 Optical and electrical properties of MoS<sub>2</sub> and HP-MoS<sub>2</sub>.** **a** PL spectra of MoS<sub>2</sub> and HP-MoS<sub>2</sub> with different treatment times, showing quenching behavior. Inset shows a change of PL intensity at 1.8 eV. **b** PL spectra fitting result with increasing plasma treatment time. The intensity of PL spectra is normalized to maximum intensity. **c** Spectral weight and photon energy of PL peak contributions as a function of treatment time. **d** Output curves ( $I_{ds}$ - $V_{ds}$ ) of MoS<sub>2</sub> FETs under 80 V of back gate voltage ( $V_{bg}$ ) with increasing treatment time. The contact area of MoS<sub>2</sub> device was covered by PMMA to prevent damage of MoS<sub>2</sub> under metal electrodes. The inset shows optical image of fabricated FET.

broad strips with the reduced intervals as shown in Fig. 7e, f. The line profile shows losing periodicity between lattice point in HP-MoS<sub>2</sub> (Fig. 7g). Sharp peaks were observed in as-grown MoS<sub>2</sub>, while periodic distance became broader in HP-MoS<sub>2</sub> (10 min) and nearly disappeared in HP-MoS<sub>2</sub> (30 min). Nevertheless, the surface roughness of the HP-MoS<sub>2</sub> is similar to that of the as-grown MoS<sub>2</sub> irrespective of the plasma treatment time (Fig. 7h). Even though the surface roughness increased somewhat from  $\sim 0.003$  nm (for as-grown) to  $\sim 0.03$  nm (for 10- and 30 min-treated ones), the topographical change is still negligible compared to the nominal step height of MoS<sub>2</sub> ( $\sim 0.65$  nm).

In addition, the lateral stiffness of the as-grown MoS<sub>2</sub> measured from the regular sawtooth patterns of the friction loop was  $15 \pm 2.3$  mV/nm (Fig. 7i). However, the prolonged plasma treatment increased the lateral stiffness to  $22.9 \pm 16.7$  mV/nm for the HP-MoS<sub>2</sub> treated for 10 min, finally leading to no detectable sawtooth pattern for the HP-MoS<sub>2</sub> treated for 30 min.

The measured total lateral stiffness ( $k_{tot}$ ) is described as

$$\frac{1}{k_{tot}} = \frac{1}{k_{lever}} + \frac{1}{k_{cont}} \quad (1)$$

where  $k_{lever}$  and  $k_{cont}$  are the lateral stiffness of cantilever and tip-sample contact, respectively<sup>67</sup>. When the tip approaches, the surface of MoS<sub>2</sub>,  $k_{cont}$  is approximated as the out-of-bending

stiffness of 2D layer ( $K_{2D, bend}$ ), so that  $k_{tot}$  is governed by the weakest spring<sup>68</sup>. As shown in Fig. 7i, we can clearly observe the stick-slip from as-grown MoS<sub>2</sub> at atomic scale, meaning that the effect of tip-sample contact is dominant factor as we discussed. However, in the HP-MoS<sub>2</sub>, the stick-slip was weakened as  $\eta$  decreased below 1 due to reduced contribution of  $k_{cont}$  to  $k_{tot}$ . This indicates that HP-MoS<sub>2</sub> has the increased out-of-bending stiffness. Instead, the effect of  $k_{lever}$  becomes dominant in Eq. (1), leading to dramatic increase in the average friction of MoS<sub>2</sub>. The friction ratio between MoS<sub>2</sub> and SiO<sub>2</sub> (see Supplementary Fig. 4a for friction ratio of MoS<sub>2</sub> to the surrounding SiO<sub>2</sub>), shows that as-grown MoS<sub>2</sub> is less sticky than SiO<sub>2</sub> substrate, while the drastic reversion was observed in HP-MoS<sub>2</sub> (30 min) due to enhanced cantilever bending effect at defective surface. In addition, the energy dissipation calculated from the area of the friction loop shows increasing fluctuation after treatment as depicted in Supplementary Fig. 4b, which is in agreement with that such high fluctuation occurs in the vicinity of sulfur vacancy of monolayer MoS<sub>2</sub><sup>69</sup>.

According to structural characterization, we confirmed that the indirect hydrogen plasma primarily generates sulfur vacancies in the topmost surface of MoS<sub>2</sub> without harming its basal plane. Furthermore, defects and defect-induced strain in MoS<sub>2</sub> affect optical, electrical, and mechanical properties.

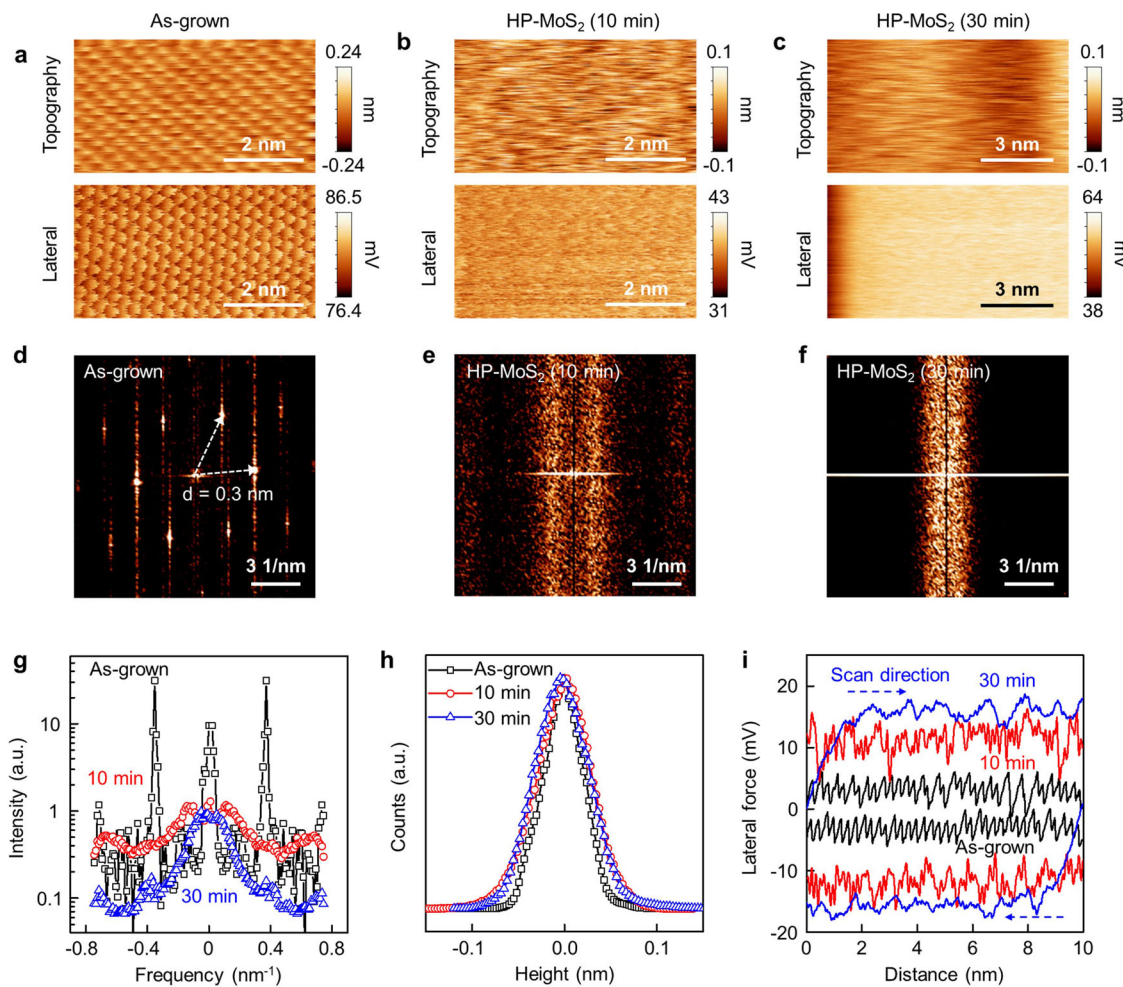


**Fig. 7 Atomic scale local frictional properties of HP-MoS<sub>2</sub>.** **a-c** Topography and lateral force images of as-grown MoS<sub>2</sub>, HP-MoS<sub>2</sub> (10 min), and HP-MoS<sub>2</sub> (30 min), respectively. **d-f** Diffraction patterns obtained from lateral force image of MoS<sub>2</sub>, HP-MoS<sub>2</sub> (10 min), and HP-MoS<sub>2</sub> (30 min), respectively. **g** The line profile of frequencies extracted from **d** to **f**. **h** The height distributions of MoS<sub>2</sub> samples. The similar shape of three curves indicates the uniform surface despite the defective structure of HP-MoS<sub>2</sub>. **i** Representative friction loop obtained during a single scan.

## Conclusion

We observed the evolution of defect formation during the desulfurization process, especially, one-atom-thick removal of sulfur atoms in three-atom-thick monolayer MoS<sub>2</sub>. We exposed low-energy remote hydrogen plasma to demonstrate atomic structure and chemical composition of monolayer MoS<sub>2</sub> with a mild manner, which allow us to observe changes systematically with atomic precision. The detailed analysis revealed that low-energy plasma leads to generate sulfur vacancies at the topmost surface of MoS<sub>2</sub>, and both molybdenum and sulfur atoms in lower layers remained intact. In addition, cracks along the zigzag edge of MoS<sub>2</sub> appeared during the relaxation of defect-induced biaxial tensile strain when sulfur vacancies possessed half of the topmost sulfur layer. We believe that our observations provide information on the evolution of atomic structure during surface engineering process and potential of plasma-based precise surface modification techniques of TMDs. Such modulation of defect could be further extended potential of MoS<sub>2</sub> and other TMDs for future electronics and catalytic reactions.

## Methods

**Sample synthesis.** Monolayer MoS<sub>2</sub> on SiO<sub>2</sub> (285 nm)/Si substrate was synthesized using an APCVD (atmospheric pressure CVD) system. Before the growth process, substrates (2.3 × 2.3 cm<sup>2</sup>) were cleaned via sonication in acetone and isopropyl alcohol for 10 min each. Molybdenum trioxide powder (MoO<sub>3</sub>, 3 mg,

Sigma-Aldrich) loaded quartz boat was heated to 750 °C at center of the furnace. Another quartz boat filled with sulfur powder (S, 180 mg, Sigma-Aldrich) was placed at 23 cm away from the center toward the upstream (temperature of sulfur is measured as 220 °C). The substrate was positioned upside-down on MoO<sub>3</sub> powder filled quartz boat. The temperature of furnace was ramping up to the reaction temperature of 750 °C with a ramping rate of 50 °C /min. Reaction maintained for 15 min with supplying Ar gas (300 sccm) for carrying sulfur and MoO<sub>3-x</sub> vapors to the substrate. After growth, the furnace was cooled naturally to 600 °C, followed by rapid cooling.

**Plasma treatment.** The hydrogen plasma treatment was performed using home-built indirect plasma system (L-Gen; Femto Science), which is embedded in conventional CVD system. The plasma generator is composed of three electrodes and power generator, whose adjustable parameters are generation power and time. In three electrodes configuration, electrodes at both ends are connected to ground, and center electrode is worked as low-frequency electrode for plasma generation, respectively. This plasma generator is movable along quartz tube to control plasma-to-sample distance. Owing to the plasma-to-sample distance, plasma generation area and target sample are separated along the reaction chamber. Thus, MoS<sub>2</sub> is exposed to the reactive plasma species with a minimized bombardment effect, which realizes 'indirect' hydrogen plasma treatment. The target sample was located 3 cm away from plasma ignition for indirect plasma treatment. The plasma generation power was 20 W with 50 kHz of fixed frequency, and hydrogen gas flow was 20 sccm ( $1.2 \times 10^{-1}$  Torr).

**Structural characterizations.** The optical properties (Raman and PL) of the MoS<sub>2</sub> were measured using Raman spectroscope (inVia; Renishaw) with a wavelength of 532 nm and a spot size of 1 μm. To prevent the degradation of samples during measurement, the laser power (2.2 mW) was carefully chosen. Both Raman and PL

spectra at the same position on  $\text{MoS}_2$  before and after plasma treatment were obtained. Observation of the surface morphology of  $\text{MoS}_2$  and HP- $\text{MoS}_2$ , SEM (VEGA 3; Tescan) was used under 30 kV of acceleration voltage, and AFM (NX-10; Park Systems) was used under contact mode. To investigate tribological variation of  $\text{MoS}_2$  with different treatment time, high-resolution AFM (Cypher ES; Oxford Instruments) was utilized under contact mode. In order to make more accurate comparison, the loading force of tip was maintained at 2 nN for every measurement, and the fast scan direction was oriented parallel to one edge of each triangular  $\text{MoS}_2$  single crystal and the scan velocity was fixed at 20 nm/sec. The root-mean square roughness values ( $R_{\text{rms}}$ ) were determined by scanning more than a few different regions for each sample. Considering the atomically smooth surface of samples,  $\sim 100 \text{ nm} \times \sim 100 \text{ nm}$  areas were scanned.

**Transmission electron microscopy measurements.** To prepare graphene support film for TEM and STEM measurement, CVD-grown graphene was transferred on holey carbon film deposited TEM grid (Quantifoil) by a direct transfer method<sup>70</sup>. TEM grid was placed on graphene grown Cu foil, and droplet of isopropyl alcohol was dropped on the surface of TEM grid. After evaporation of isopropyl alcohol naturally, the sample was floated on copper etchant (0.1 M ammonium persulfate solution) for 2–3 h. The copper etched graphene/TEM grid was sequentially moved to deionized water to remove residual chemical several times and dried naturally. The CVD-grown  $\text{MoS}_2$  on  $\text{SiO}_2$  substrate was located on as-prepared graphene-coated holey carbon TEM grid for Fig. 2a–d or silicon nitride membrane (PELCO) for Fig. 3g, h using PDMS stamp method<sup>71</sup>. TEM and STEM imaging were performed by an atomic resolution TEM (JEM-ARM200F; JEOL) equipped with image and probe aberration correctors operated at 80 kV. HAADF-STEM images were obtained with a convergence angle of 23 mrad and the collection semi-angles from 40 to 160 mrad. ImageJ and Gatan Digital Micrograph were used to process the HAADF images.

**Electrical characterizations.** To fabricate  $\text{MoS}_2$ -based FETs using CVD-grown  $\text{MoS}_2$  on  $\text{SiO}_2$  substrate, source and drain electrodes were defined by an e-beam lithography using a nanolithography system (PIONEER 2; Raith). We deposited metal electrodes (Al 20 nm/Cr 5 nm/Au 30 nm) with an e-beam evaporator (Korea Vacuum Tech.) in a high vacuum of  $10^{-8}$  Torr. The lift-off process was performed in acetone. Electrical measurements were carried out by semiconductor parameter analyzer (Keithley 4200; Keithley) at room temperature under ambient condition.

**Chemical characterizations.** The chemical composition of  $\text{MoS}_2$  and HP- $\text{MoS}_2$  was performed by AES and ToF-SIMS. The AES data were obtained by Auger nanoprobe (PHI 700; ULVAC-PHI) equipped with cylindrical mirror analyzer (energy resolution  $< 0.5\%$ ). The base pressure is under  $5 \times 10^{-10}$  Torr. To avoid the charging effect of  $\text{SiO}_2$  substrate, the samples were tilted during measurement process. The electron beam current of 10 nA with an acceleration voltage of 3 kV was used. The quantitative analysis of sulfur and molybdenum atoms was performed using sensitive factors derived from as-synthesized  $\text{MoS}_2$  to directly compare the effect of sulfur vacancy generation. ToF-SIMS (TOF.SIMS-5; ION-TOF) was performed in negative mode using a Bismuth primary ion beam at 30 keV of beam energy with 1 pA of current. The sputtering was processed using a Cs at 0.5 keV of beam energy with 40 nA of current to achieve depth profile. The measurements were performed using facilities of the Korea Institute of Science and Technology (Seoul, South Korea).

## Data availability

The data that support plots and related finding of this work are available from the corresponding author upon reasonable request.

Received: 21 January 2021; Accepted: 5 July 2021;

Published online: 23 July 2021

## References

- Qiu, H. et al. Hopping transport through defect-induced localized states in molybdenum disulphide. *Nat. Commun.* **4**, 2642 (2013).
- Ma, J.-J., Zheng, J.-J., Li, W.-D., Wang, D.-H. & Wang, B.-T. Thermal transport properties of monolayer  $\text{MoSe}_2$  with defects. *Phys. Chem. Chem. Phys.* **22**, 5832–5838 (2020).
- Zhang, G. & Zhang, Y.-W. Thermoelectric properties of two-dimensional transition metal dichalcogenides. *J. Mater. Chem. C* **5**, 7684–7698 (2017).
- Tongay, S. et al. Defects activated photoluminescence in two-dimensional semiconductors: interplay between bound, charged, and free excitons. *Sci. Rep.* **3**, 2657 (2013).
- Chen, Y. et al. Tuning electronic structure of single layer  $\text{MoS}_2$  through defect and interface engineering. *ACS Nano* **12**, 2569–2579 (2018).
- Mahata, A., Jiang, J.-W., Mahapatra, D. R. & Rabczuk, T. Effect of intrinsic structural defects on mechanical properties of single layer  $\text{MoS}_2$ . *Nano-Struct. Nano-Objects* **18**, 100247 (2019).
- Hasanian, M., Mortazavi, B., Ostadhosseini, A., Rabczuk, T. & van Duin, A. C. T. Hydrogenation and defect formation control the strength and ductility of  $\text{MoS}_2$  nanosheets: Reactive molecular dynamics simulation. *Extreme Mech. Lett.* **22**, 157–164 (2018).
- Nan, H. et al. Strong photoluminescence enhancement of  $\text{MoS}_2$  through defect engineering and oxygen bonding. *ACS Nano* **8**, 5738–5745 (2014).
- Liu, H. & Chi, D. Dispersive growth and laser-induced rippling of large-area singlelayer  $\text{MoS}_2$  nanosheets by CVD on c-plane sapphire substrate. *Sci. Rep.* **5**, 11756 (2015).
- Komsa, H.-P. et al. Two-dimensional transition metal dichalcogenides under electron irradiation: defect production and doping. *Phys. Rev. Lett.* **109**, 035503 (2012).
- Tapaszto, L. et al. Tuning the electronic structure of graphene by ion irradiation. *Phys. Rev. B* **78**, 233407 (2008).
- Tosun, M. et al. Air-stable n-doping of  $\text{WSe}_2$  by anion vacancy formation with mild plasma treatment. *ACS Nano* **10**, 6853–6860 (2016).
- Kim, S. et al. Effects of plasma treatment on surface properties of ultrathin layered  $\text{MoS}_2$ . *2D Mater.* **3**, 035002 (2016).
- Xiao, S. et al. Atomic-layer soft plasma etching of  $\text{MoS}_2$ . *Sci. Rep.* **6**, 19945 (2016).
- Chen, M. et al. Stable few-layer  $\text{MoS}_2$  rectifying diodes formed by plasma-assisted doping. *Appl. Phys. Lett.* **103**, 142110 (2013).
- Alexeev, A. M., Barnes, M. D., Nagareddy, V. K., Craciun, M. F. & Wright, C. D. A simple process for the fabrication of large-area CVD graphene based devices via selective in situ functionalization and patterning. *2D Mater.* **4**, 011010 (2016).
- Wang, X. et al. Single-atom vacancy defect to trigger high-efficiency hydrogen evolution of  $\text{MoS}_2$ . *J. Am. Chem. Soc.* **142**, 4298–4308 (2020).
- Tsai, C. et al. Electrochemical generation of sulfur vacancies in the basal plane of  $\text{MoS}_2$  for hydrogen evolution. *Nat. Commun.* **8**, 15113 (2017).
- Yin, Y. et al. Contributions of phase, sulfur vacancies, and edges to the hydrogen evolution reaction catalytic activity of porous molybdenum disulfide nanosheets. *J. Am. Chem. Soc.* **138**, 7965–7972 (2016).
- Ostrikov, K., Neyts, E. C. & Meyappan, M. Plasma nanoscience: from nanosolids in plasmas to nano-plasmas in solids. *Adv. Phys.* **62**, 113–224 (2013).
- Nan, H. et al. Soft hydrogen plasma induced phase transition in monolayer and few-layer  $\text{MoTe}_2$ . *Nanotechnology* **30**, 034004 (2019).
- Ye, G. et al. Defects engineered monolayer  $\text{MoS}_2$  for improved hydrogen evolution reaction. *Nano Lett.* **16**, 1097–1103 (2016).
- Cheng, C.-C. et al. Activating basal-plane catalytic activity of two-dimensional  $\text{MoS}_2$  monolayer with remote hydrogen plasma. *Nano Energy* **30**, 846–852 (2016).
- Li, R., Cheng, Y. & Huang, W. Recent progress of Janus 2D transition metal dichalcogenides: from theory to experiments. *Small* **14**, 1802091 (2018).
- Zhang, L. et al. Recent advances in emerging Janus two-dimensional materials: from fundamental physics to device applications. *J. Mater. Chem. A* **8**, 8813–8830 (2020).
- Lu, A. Y. et al. Janus monolayers of transition metal dichalcogenides. *Nat. Nanotechnol.* **12**, 744–749 (2017).
- Trivedi, D. B. et al. Room-temperature synthesis of 2D Janus crystals and their heterostructures. *Adv. Mater.* **32**, 2006320 (2020).
- Cheng, Y. et al. Defects enhance the electrocatalytic hydrogen evolution properties of  $\text{MoS}_2$ -based materials. *Chem. Asian J.* **15**, 3123–3134 (2020).
- Li, L. et al. Role of sulfur vacancies and undercoordinated Mo regions in  $\text{MoS}_2$  nanosheets toward the evolution of hydrogen. *ACS Nano* **13**, 6824–6834 (2019).
- Le, D., Rawal, T. B. & Rahman, T. S. Single-layer  $\text{MoS}_2$  with sulfur vacancies: structure and catalytic application. *J. Phys. Chem. C* **118**, 5346–5351 (2014).
- Han, S. W., Cha, G.-B., Kim, K. & Hong, S. C. Hydrogen interaction with a sulfur-vacancy-induced occupied defect state in the electronic band structure of  $\text{MoS}_2$ . *Phys. Chem. Chem. Phys.* **21**, 15302–15309 (2019).
- Son, J. et al. Tunable wettability of graphene through nondestructive hydrogenation and wettability-based patterning for bioapplications. *Nano Lett.* **20**, 5625–5631 (2020).
- Son, J. et al. Hydrogenated monolayer graphene with reversible and tunable wide band gap and its field-effect transistor. *Nat. Commun.* **7**, 13261 (2016).
- Moschetta, M. et al. Hydrogenated graphene improves neuronal network maturation and excitatory transmission. *Adv. Biol.* **5**, 2000177 (2021).
- van der Zande, A. M. et al. Grains and grain boundaries in highly crystalline monolayer molybdenum disulphide. *Nat. Mater.* **12**, 554–561 (2013).
- Mignuzzi, S. et al. Effect of disorder on Raman scattering of single-layer  $\text{MoS}_2$ . *Phys. Rev. B* **91**, 195411 (2015).
- Parkin, W. M. et al. Raman shifts in electron-irradiated monolayer  $\text{MoS}_2$ . *ACS Nano* **10**, 4134–4142 (2016).

38. Oh, H. M. et al. Photochemical reaction in monolayer MoS<sub>2</sub> via correlated photoluminescence, Raman spectroscopy, and atomic force microscopy. *ACS Nano* **10**, 5230–5236 (2016).
39. Jadwiszczak, J. et al. Oxide-mediated recovery of field-effect mobility in plasma-treated MoS<sub>2</sub>. *Sci. Adv.* **4**, eaao5031 (2018).
40. Ko, T. Y. et al. On-stack two-dimensional conversion of MoS<sub>2</sub> into MoO<sub>3</sub>. *2D Mater.* **4**, 014003 (2016).
41. Stanford, M. G. et al. Lithographically patterned metallic conduction in single-layer MoS<sub>2</sub> via plasma processing. *npj 2D Mater. Appl.* **3**, 13 (2019).
42. Panthani, M. G. et al. Graphene-supported high-resolution TEM and STEM imaging of silicon nanocrystals and their capping Ligands. *J. Phys. Chem. C* **116**, 22463–22468 (2012).
43. Pennycook, S. J. & Nellist, P. D. (eds) *Scanning transmission electron microscopy: Imaging and Analysis*. (Springer, 2011).
44. Vancsó, P. et al. The intrinsic defect structure of exfoliated MoS<sub>2</sub> single layers revealed by Scanning Tunneling Microscopy. *Sci. Rep.* **6**, 29726 (2016).
45. Hong, J. et al. Exploring atomic defects in molybdenum disulphide monolayers. *Nat. Commun.* **6**, 6293 (2015).
46. Shree, S. et al. High optical quality of MoS<sub>2</sub> monolayers grown by chemical vapor deposition. *2D Mater.* **7**, 015011 (2019).
47. Wang, L., Ji, X., Chen, F. & Zhang, Q. Temperature-dependent properties of monolayer MoS<sub>2</sub> annealed in an Ar diluted S atmosphere: an experimental and first-principles study. *J. Mater. Chem. C* **5**, 11138–11143 (2017).
48. Han, Y., Hu, T., Li, R., Zhou, J. & Dong, J. Stabilities and electronic properties of monolayer MoS<sub>2</sub> with one or two sulfur line vacancy defects. *Phys. Chem. Chem. Phys.* **17**, 3813–3819 (2015).
49. Wang, S., Lee, G. D., Lee, S., Yoon, E. & Warner, J. H. Detailed atomic reconstruction of extended line defects in monolayer MoS<sub>2</sub>. *ACS Nano* **10**, 5419–5430 (2016).
50. Pierucci, D. et al. Tunable doping in hydrogenated single layered molybdenum disulfide. *ACS Nano* **11**, 1755–1761 (2017).
51. Li, D. et al. MoS<sub>2</sub> memristors exhibiting variable switching characteristics toward biorealistic synaptic emulation. *ACS Nano* **12**, 9240–9252 (2018).
52. Liang, F. et al. Raman spectroscopy characterization of two-dimensional materials. *Chin. Phys. B* **27**, 037802 (2018).
53. Hui, Y. Y. et al. Exceptional tunability of band energy in a compressively strained trilayer MoS<sub>2</sub> sheet. *ACS Nano* **7**, 7126–7131 (2013).
54. Lloyd, D. et al. Band gap engineering with ultralarge biaxial strains in suspended monolayer MoS<sub>2</sub>. *Nano Lett.* **16**, 5836–5841 (2016).
55. Chow, P. K. et al. Defect-induced photoluminescence in monolayer semiconducting transition metal dichalcogenides. *ACS Nano* **9**, 1520–1527 (2015).
56. Kang, N., Paudel, H. P., Leuenberger, M. N., Tetard, L. & Khondaker, S. I. Photoluminescence quenching in single-layer MoS<sub>2</sub> via oxygen plasma treatment. *J. Phys. Chem. C* **118**, 21258–21263 (2014).
57. McCreary, K. M., Hanbicki, A. T., Sivaram, S. V. & Jonker, B. T. A- and B-exciton photoluminescence intensity ratio as a measure of sample quality for transition metal dichalcogenide monolayers. *APL Mater.* **6**, 111106 (2018).
58. Yang, L. et al. Lattice strain effects on the optical properties of MoS<sub>2</sub> nanosheets. *Sci. Rep.* **4**, 5649 (2014).
59. Scalise, E., Houssa, M., Pourtois, G., Afanas'ev, V. & Stesmans, A. Strain-induced semiconductor to metal transition in the two-dimensional honeycomb structure of MoS<sub>2</sub>. *Nano Res.* **5**, 43–48 (2012).
60. Cai, Y. et al. Constructing metallic nanoroads on a MoS<sub>2</sub> monolayer via hydrogenation. *Nanoscale* **6**, 1691–1697 (2014).
61. Adessi, C., Pecorario, S., Thébaud, S. & Bouzerar, G. First principle investigation of the influence of sulfur vacancies on thermoelectric properties of single layered MoS<sub>2</sub>. *Phys. Chem. Chem. Phys.* **22**, 15048–15057 (2020).
62. Chee, S.-S. et al. Sulfur vacancy-induced reversible doping of transition metal disulfides via hydrazine treatment. *Nanoscale* **9**, 9333–9339 (2017).
63. Wang, Q. H., Kalantar-Zadeh, K., Kis, A., Coleman, J. N. & Strano, M. S. Electronics and optoelectronics of two-dimensional transition metal dichalcogenides. *Nat. Nanotechnol.* **7**, 699–712 (2012).
64. Cahangirov, S., Ataca, C., Topsakal, M., Sahin, H. & Ciraci, S. Frictional figures of merit for single layered nanostructures. *Phys. Rev. Lett.* **108**, 126103 (2012).
65. Gnecco, E., Bennewitz, R., Gyalog, T. & Meyer, E. Friction experiments on the nanometre scale. *J. Condens. Matter Phys.* **13**, R619–R642 (2001).
66. Socoliuc, A., Bennewitz, R., Gnecco, E. & Meyer, E. Transition from stick-slip to continuous sliding in atomic friction: entering a new regime of ultralow friction. *Phys. Rev. Lett.* **92**, 134301 (2004).
67. Carpick, R. W., Ogletree, D. F. & Salmeron, M. Lateral stiffness: a new nanomechanical measurement for the determination of shear strengths with friction force microscopy. *Appl. Phys. Lett.* **70**, 1548–1550 (1997).
68. Kwon, S., Ko, J.-H., Jeon, K.-J., Kim, Y.-H. & Park, J. Y. Enhanced nanoscale friction on fluorinated graphene. *Nano Lett.* **12**, 6043–6048 (2012).
69. Pang, H., Wang, H., Li, M. & Gao, C. Atomic-scale friction on monovacancy-defective graphene and single-layer molybdenum-disulfide by numerical analysis. *Nanomaterials* **10**, 87 (2020).
70. Regan, W. et al. A direct transfer of layer-area graphene. *Appl. Phys. Lett.* **96**, 113102 (2010).
71. Castellanos-Gomez, A. et al. Deterministic transfer of two-dimensional materials by all-dry viscoelastic stamping. *2D Mater.* **1**, 011002 (2014).

## Acknowledgements

This work was supported by the Basic Science Research Program through the National Research Foundation of Korea (2017R1A5A1014862, 2018M3D1A1058793, 2021H1D3A2A01045033) and Creative-Pioneering Researchers Program through Seoul National University (SNU) (21A20131912052). Y.L. and K.K. acknowledge support from the Basic Science Research Program through the National Research Foundation of Korea (NRF-2017R1A5A1014862) and the Institute for Basic Science (IBS-R026-D1). A.M.v.d.Z. acknowledges support from NSF-MRSEC under award number DMR-1720633. J.S. was supported by the National Research Council of Science & Technology (NST) grant by the Korea government (MSIT) (No. CRC-20-01-NRFI) and the National Research Foundation of Korea (NRF) funded by the Ministry of Science and ICT (NRF-2021M3H4A1A01079358).

## Author contributions

J.L., J.H.K., J.S., and G.H.L. conceived and designed the study. J.L. and J.H.K. prepared samples and carried out experiments under the guidance of J.S., G.H.L., and with the help of the other authors. Y.J. and J.C.S. assisted in the synthesis of MoS<sub>2</sub> samples. Y.L. and K. K. executed the TEM and STEM experiments. N.K. and A.M.v.d.Z. contributed to the discussion of the paper. All authors discussed the results and commented on the manuscript.

## Competing interests

The authors declare no competing interests.

## Additional information

**Supplementary information** The online version contains supplementary material available at <https://doi.org/10.1038/s43246-021-00185-4>.

**Correspondence** and requests for materials should be addressed to J.S. or G.-H.L.

**Peer review information** *Communications Earth & Environment* thanks the anonymous reviewers for their contribution to the peer review of this work. Primary Handling Editors: Aldo Isidori.

**Reprints and permission information** is available at <http://www.nature.com/reprints>

**Publisher's note** Springer Nature remains neutral with regard to jurisdictional claims in published maps and institutional affiliations.



**Open Access** This article is licensed under a Creative Commons Attribution 4.0 International License, which permits use, sharing, adaptation, distribution and reproduction in any medium or format, as long as you give appropriate credit to the original author(s) and the source, provide a link to the Creative Commons license, and indicate if changes were made. The images or other third party material in this article are included in the article's Creative Commons license, unless indicated otherwise in a credit line to the material. If material is not included in the article's Creative Commons license and your intended use is not permitted by statutory regulation or exceeds the permitted use, you will need to obtain permission directly from the copyright holder. To view a copy of this license, visit <http://creativecommons.org/licenses/by/4.0/>.

© The Author(s) 2021